Supporting Information

Pathak and Kumar 10.1073/pnas.1118073109

SI Methods.

Fabrication of Polyacrylamide (PA) Microchannels. Silicon masters were fabricated using standard photolithographic techniques (Fig. S1). Briefly, a silicon wafer was coated with a 25-μm-thick layer of photoresist (SU-8 2015, Microchem) and photopatterned using UV exposure through a transparency mask with predesigned micron-scale topographical features. The silicon-SU8 mold was subsequently silanized (*N*-octadecyltriethoxysilane, UCT) under vacuum, which renders the wafer hydrophobic and facilitates peeling from the polymerized PA gel. Next, a volume of PA precursor solution sufficient to achieve a gel of approximately 100 μm thickness was placed between a reactive glass surface and the hydrophobic silicon mold and allowed to polymerize. After approximately 30 min, the polymerized PA and coverslip assembly was peeled from the hydrophobic silicon-SU8 mold, resulting in transfer of the microchannel patterns onto the PA gel surface. Channel widths, c_w, are reported with respect to the silicon master, not the final PA channels; differences in channel widths ($c_w = 10$, 20, and 40 μm) were chosen to be much larger than any expected deviations from the lateral geometry of the master due to gel swelling (1). The PA solution precursor solutions were made as previously described (2) acrylamide/bisacrylamide (A/B) percentages of 4% A/0.2% B, 10% A/0.3% B, and 15% A/1.2% B corresponding to PA gels of elastic moduli of 0.4, 10, and 120 kPa (2, 3). All substrates were functionalized with human plasma fibronectin (Millipore) to achieve a nominal surface density of 2.5 $\mu g/cm^2$.

Cell Culture. U373-MG human glioma cells were cultured as previously described (2) in DMEM (Invitrogen) containing 10% calf serum (JR Scientific), 1% MEM nonessential amino acids (Invitrogen), 1% penicillin/streptomycin (Invitrogen), and 1% sodium pyruvate (Invitrogen). Cells were seeded on PA gels with embedded channels at a subconfluent density of 3000 cells per cm^2 at least 8 h prior to the start of imaging and data acquisition. The NMMII inhibitor blebbistatin (Sigma-Aldrich) was added to the cell culture medium at 10 μM final concentration in relevant experiments at least 12 h after initial cell seeding.

Live Cell Imaging and Data Analysis. Live cell imaging was performed using a Nikon TE2000E2 microscope equipped with an incubator chamber for controlled temperature, humidity, and CO_2, and a motorized, programmable stage (Prior Scientific, Inc.). Images were recorded with a CCD camera (Photometrics Coolsnap HQ2) interfaced to image acquisition software (SimplePCI, Hamamatsu Corporation). In each experiment, 10x phase contrast images were acquired every 10 min for 10–12 h. Migration speeds were quantified using manual tracking in ImageJ (National Institutes of Health). The data were further processed to obtain a mean speed for a given condition. Cell spreading areas were measured using ImageJ by manually tracing the projected outlines of 30–50 cells per condition. Aspect ratios were calculated as the ratio of major axis/minor axis length using the shape analysis feature in ImageJ.

Immunofluorescence, Confocal Microscopy, and Image Analysis. Cells were fixed with 4% paraformaldehyde (Fisher Scientific) in PBS, followed by permeabilization of cell membrane with 0.1% Triton-X 100 (EMD Biosciences) and blocking with 5% goat serum in PBS. Subsequently, cellular F-actin was stained with Alexa Fluor 488 phalloidin (Invitrogen; diluted 1:200). The following antibodies were used for immunofluorescence: mouse monoclonal anti-vinculin IgG (Sigma-Aldrich; diluted 1:200), rabbit polyclonal phosphomyosin light chain 2-Ser19 (Cell Signaling; diluted 1:200), and Alexa Fluor 546-labeled goat anti-mouse and goat anti-rabbit (Invitrogen; diluted 1:250). Confocal images (60X) were captured with an Olympus BX51WI microscope (Olympus Corporation) equipped with Swept Field Confocal technology (Prairie Technologies, Inc.), and z-stacks were acquired at an interval of 1 μm. The z-stacks for each cell were combined in ImageJ (NIH) using the Z-Project tool. The resulting z-projected image of actin distribution for each cell was analyzed using OrientationJ algorithm (4) implemented in ImageJ. The degree of stress fiber alignment for each cell was measured in terms of coherency in OrientationJ, which varies between 0, indicating isotropic distribution, and 1, indicating highly aligned structures.

Statistical Analysis. Except where noted, data are reported as mean ± standard error, and statistical comparisons were performed with a one-way ANOVA followed by a Tukey-Kramer HSD (honestly significant difference) test for pairwise comparisons.

Atomic Force Microscopy. Measurements were acquired with an MFP-3D atomic force microscope (Asylum Research) by indenting the gels using pyramid-tipped probes (SNL or OTR4; Bruker AFM Probes) with spring constants of 150–275 pN/nm, as measured by thermal calibration. Elastic moduli were extracted from force curves using a modified Hertz model (5).

Mathematical Model Integrating Subcellular Processes and Cell Migration. Our model assumes that cell migration is a result of several subcellular mechanisms working in tandem: stabilization of adhesions, extension of protrusions, and generation of actomyosin contractility to overcome drag forces (6–8). In all cases, we report steady-state relationships that capture the interdependence of these processes and their relations to ECM properties (Fig. S3).

Adhesions and cell spreading. We start with a description for cell spreading supported primarily by cell-ECM adhesions, which are known to grow with ECM stiffness through mechanochemical feedback (7, 9, 10). We use the thermodynamic equilibrium between closed and open receptor-ligand bonds as a guideline to derive a relationship between adhesion size and ECM stiffness (11–13). Here, the work done by contractile force, balanced by ECM rigidity, reduces the free energy of the closed bonds and stabilizes the focal adhesions, which in turn increases the size of adhesions. A steady-state balance of free energy of open (on the left) and closed (on the right) receptor-ligand bonds can be written as

$$\ln\left(\frac{1-n_c}{k_B T}\right) = \ln\left(\frac{n_c}{k_B T}\right) + \phi_o - W, \qquad \textbf{[S1]}$$

where $\phi_o = k_B T$ is the difference in reference potentials between open and closed bonds, k_B is the Boltzmann constant, and T is the absolute temperature. The reduction in free energy of the closed bonds due to forces supported by ECM stiffness, E, is calculated as $W = E\varepsilon_o$, where constant $\varepsilon_o = 10^{-7}\ \mu m^3$ is estimated as $\varepsilon_o = \delta_c{}^2 a/h$, where δ_c is the critical bond stretch (set empirically as 10 nm) (14), a is the standard adhesion size (set as 400 nm^2) (15), and h is the reference thickness of the gel (40 μm). From Eq. **S1**, the normalized number of cell-ECM adhesions (n_c) dispersed over the entire cell body in contact with the ECM can be derived as

$$n_c = 1/\left(1+\exp\left(\frac{\phi_o - E\varepsilon_o}{k_B T}\right)\right). \qquad \textbf{[S2]}$$

Cell-ECM adhesions are vital for the process of cell spreading, and a steady-state size of the cell on a given ECM is dictated by the number of adhesions dispersed over the cell body and protrusions at the leading edge that continuously stabilize the transient adhesions. The protrusive adhesions depend on the number of cell body adhesions (n_c) and a myosin signal (μ) that is known to create pauses in actin polymerization and protrusions at the leading edge of a migrating cell (16). Based on these processes, we estimate a dimensionless index for cell size, s_c, in terms of the degree of cell-ECM adhesions (Eq. **S2**) for a given ECM stiffness as

$$s_c = s_o + n_c(5 - 4\ \mu), \qquad \textbf{[S3]}$$

where $s_o = 0.33$ is a modeling constant assigned for minimal cell size.

Contractile and protrusive forces. The contractile force generated by the actomyosin machinery increases with ECM stiffness and saturates beyond a critical stiffness (7). It is also well known that the inhibition of myosin signal by blebbistatin treatment ($0 < \mu \ll 1$) curtails actomyosin contractility (2). We utilize a modified lower order Hill function (17) to formulate the actomyosin contractile force (F_c) in terms of ECM stiffness (E) and myosin signaling (μ) as

$$F_c = F_o\mu\left[0.2 + \frac{E}{E + \mu E_o}\right], \qquad \textbf{[S4]}$$

where $E_o = 4$ kPa is a constant ECM stiffness that regulates the saturation of contractile force generation. In addition to the contractile force, protrusive forces also actively propel migration depending on the size of the leading edge that is assumed to reduce for narrower channels and a myosin signal that is known to create periodic pauses in the protrusions (16, 18). Based on these assumptions, we calculate the protrusive force as

$$F_p = F_c\left(1 + \frac{c_w}{c_o}\right)\left(\frac{1-\mu}{\mu}\right), \qquad \textbf{[S5]}$$

where $c_o = 90$ μm is a normalization constant for channel width (c_w). According to this equation, a reduction in μ due to blebbistatin treatment of the cells and unconstrained protrusions in wider channels would enhance the protrusive force, F_p.

Polarization factor. In unconstrained ECM settings, cell spreading renders the actomyosin fibrils oriented in multiple directions (Fig. S3), which in turn reduces the contribution of these forces along the direction of migration. When physically constrained between channel walls, the cell polarizes its contractile forces along the direction of migration (Fig. S3). To capture these relationships, we define a *polarized* contractile force, $F_{cp} = \psi F_c$, as a fraction of the total force generated by the actomyosin contractility (F_c in Eq. **S4**), where ψ is a polarization factor that reduces with increased spreading, assessed by the cell size , s_c (Eq. **S3**) and increases for narrower channels that physically constrain the cell and polarize the stress fibers. Based on these assumptions, the polarization factor, ψ, can be written as

$$\psi = 1 - \frac{s_c c_w}{2c_o}. \qquad \textbf{[S6]}$$

Balance of forces leads to cell migration. Cell migration is propelled by the polarized contractile force ($F_{cp} = \psi F_c$) and protrusive force (F_p), and simultaneously opposed by a drag force F_d (19), which is proportional to the migration speed (v) and drag coefficients that include contributions due to cell-ECM adhesions and a confinement force due to narrow channels. We formulate the drag force as

$$F_d = v(\lambda_a + \lambda_b s_c E + \lambda_c s_c / {c_w}^2), \qquad \textbf{[S7]}$$

where $\lambda_a = 0.025$ nN·hr/μm, $\lambda_b = 2.5 \times 10^{-6}$ μm·hr, and $\lambda_c = 0.1$ nN·μm·hr are proportionality constants for the drag coefficient contributions described above. By utilizing the balance of subcellular forces as $F_{cp} + F_p - F_d = 0$, and substituting the force components from Eqs. **S4–S7**, we derive the equation for migration speed (v) as

$$v = \frac{\psi F_c + F_p}{(\lambda_a + \lambda_b s_c E + \lambda_c s_c / {c_w}^2)}. \qquad \textbf{[S8]}$$

1. Charest JM, Califano JP, Carey SP, Reinhart-King CA (2012) Fabrication of substrates with defined mechanical properties and topographical features for the study of cell migration. *Macromol Biosci* 12:12–20.
2. Ulrich TA, de Juan Pardo EM, Kumar S (2009) The mechanical rigidity of the extracellular matrix regulates the structure, motility, and proliferation of glioma cells. *Cancer Res* 69:4167–4174.
3. Saha K, et al. (2008) Substrate modulus directs neural stem cell behavior. *Biophys J* 95:4426–4438.
4. Rezakhaniha R, et al. (2011) Experimental investigation of collagen waviness and orientation in the arterial adventitia using confocal laser scanning microscopy. *Biomech Model Mechan* 11:461–473.
5. Bilodeau GG (1992) Regular pyramid punch problem. *J Appl Mech* 59:519–523.
6. Lauffenburger DA, Horwitz AF (1996) Cell migration: A physically integrated molecular process. *Cell* 84:359–369.
7. Pathak A, Kumar S (2011) From molecular signal activation to locomotion: An integrated, multiscale analysis of cell motility on defined matrices. *PLoS ONE* 6:e18423.
8. Ridley AJ, *et al*. (2003) Cell migration: Integrating signals from front to back. *Science* 302:1704–1709.
9. Bershadsky A, Kozlov M, Geiger B (2006) Adhesion-mediated mechanosensitivity: A time to experiment, and a time to theorize. *Curr Opin Cell Biol* 18:472–481.
10. Shemesh T, Geiger B, Bershadsky AD, Kozlov MM (2005) Focal adhesions as mechanosensors: A physical mechanism. *Proc Natl Acad Sci USA* 102:12383–12388.
11. Pathak A, McMeeking RM, Evans AG, Deshpande VS (2011) An analysis of the cooperative mechano-sensitive feedback between intracellular signaling, focal adhesion development, and stress fiber contractility. *J Appl Mech* 78:041001–041012.
12. Pathak A, Deshpande VS, McMeeking RM, Evans AG (2008) The simulation of stress fibre and focal adhesion development in cells on patterned substrates. *J R Soc Interface* 5:507–524.
13. Deshpande VS, Mrksich M, McMeeking RM, Evans AG (2008) A bio-mechanical model for coupling cell contractility with focal adhesion formation. *J Mech Phys Solids* 56:1484–1510.
14. Merkel R, Nassoy P, Leung A, Ritchie K, Evans E (1999) Energy landscapes of receptor-ligand bonds explored with dynamic force spectroscopy. *Nature* 397:50–53.
15. Arnold M, et al. (2004) Activation of integrin function by nanopatterned adhesive interfaces. *ChemPhysChem* 5:383–388.
16. Giannone G, et al. (2004) Periodic lamellipodial contractions correlate with rearward actin waves. *Cell* 116:431–443.
17. Dokukina IV, Gracheva ME (2010) A model of fibroblast motility on substrates with different rigidities. *Biophys J* 98:2794–2803.
18. Vicente-Manzanares M, Zareno J, Whitmore L, Choi CK, Horwitz AF (2007) Regulation of protrusion, adhesion dynamics, and polarity by myosins IIA and IIB in migrating cells. *J Cell Biol* 176:573–580.
19. DiMilla PA, Barbee K, Lauffenburger DA (1991) Mathematical model for the effects of adhesion and mechanics on cell migration speed. *Biophys J* 60:15–37.

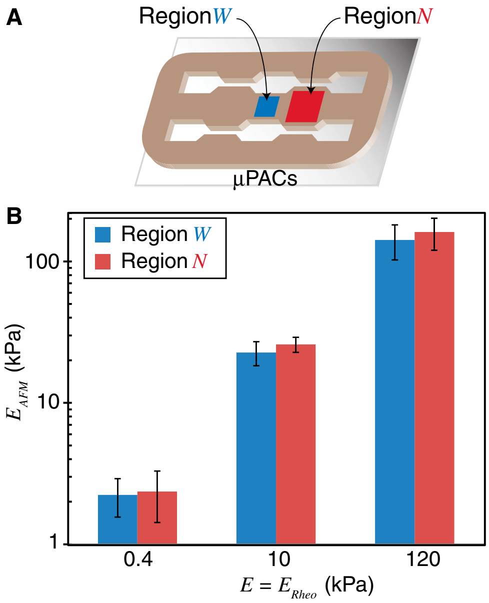

Fig. S1. Consistency of stiffness values between wide and narrow channels. (*A*) Schematic showing locations of AFM measurements, specifically wide (W) and narrow (N) plateau regions of the device. (*B*) Relationship between AFM-acquired Young's modulus (E_{AFM}) and bulk PA gel stiffness (as defined in the main text and as previously measured by parallel plate rheometry). For a given PA chemistry, the ECM stiffness does not vary between W and N regions. Data represent mean ± standard deviation.

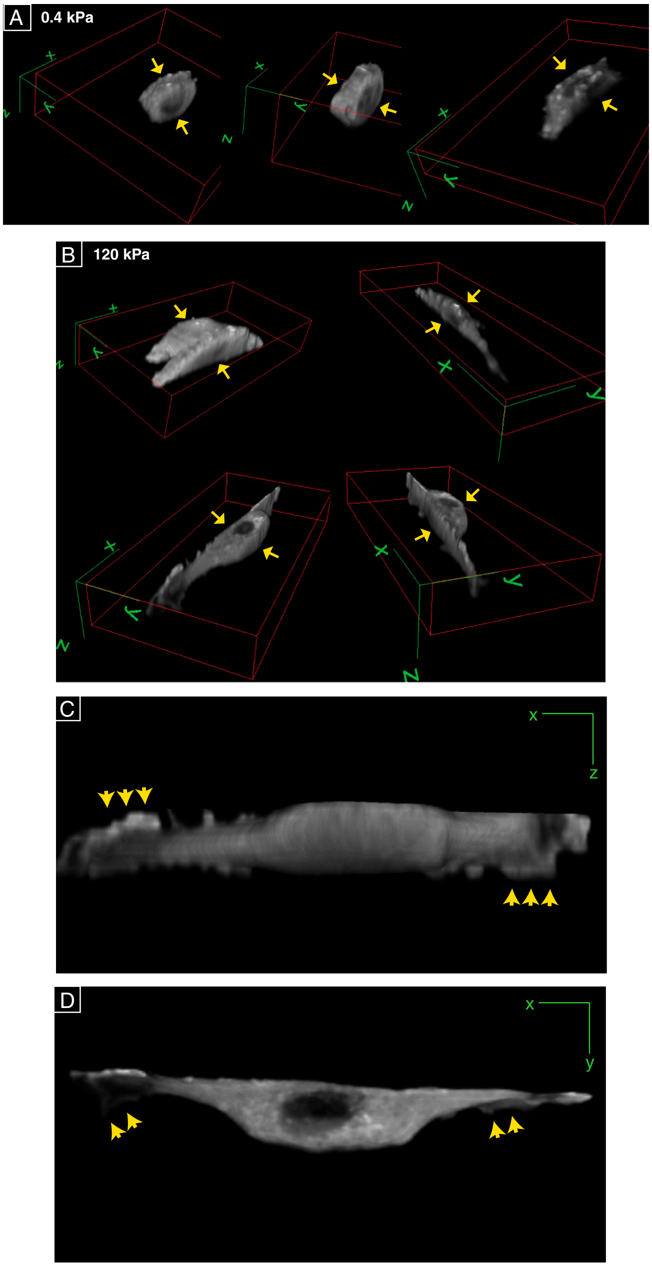

Fig. S2. Vinculin distribution for cells confined in channels. Volumetric 3D reconstruction of vinculin distributions of a cell confined inside channels fabricated from (*A*) 0.4 kPa and (*B*) 120 kPa PA hydrogels. Arrows indicate the direction of compressive confinement provided by the walls of the channel; as a result, the cell body morphs within the constraints of the 3D interior of the channel. The long axis of the channel is oriented along the *x* axis, the channel width is oriented along the *y* axis, and height is oriented along the *z* axis, with the bottom surface of the channel toward *z*. Vinculin distributions in (*C*) *x*–*z* and (*D*) *x*–*y* planes demonstrate cell spreading along a side wall of a channel made of stiff (120 kPa) PA hydrogel. Arrowheads indicate vinculin-rich protrusive processes formed along a given channel wall.

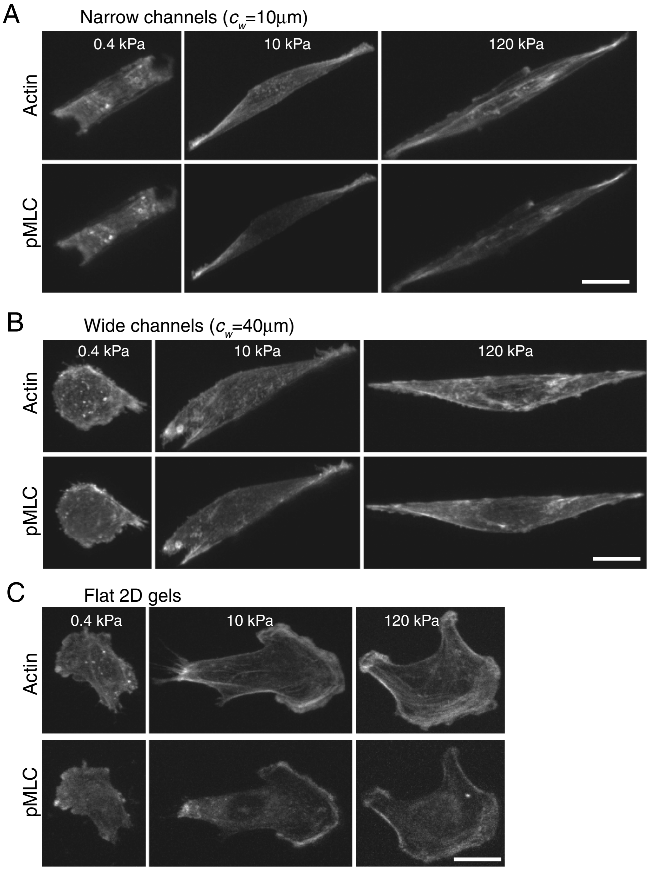

Fig. S3. Dependence of F-actin and myosin distribution on ECM stiffness and confinement. Confocal images of U373 cells fixed and stained for F-actin and phosphorylated myosin light chain (pMLC) in (*A*) narrow channels ($c_w = 10$ μm), (*B*) wide channels ($c_w = 40$ μm), and (*C*) unconfined flat 2D gels of varying ECM stiffness. Scale bar = 20 μm.

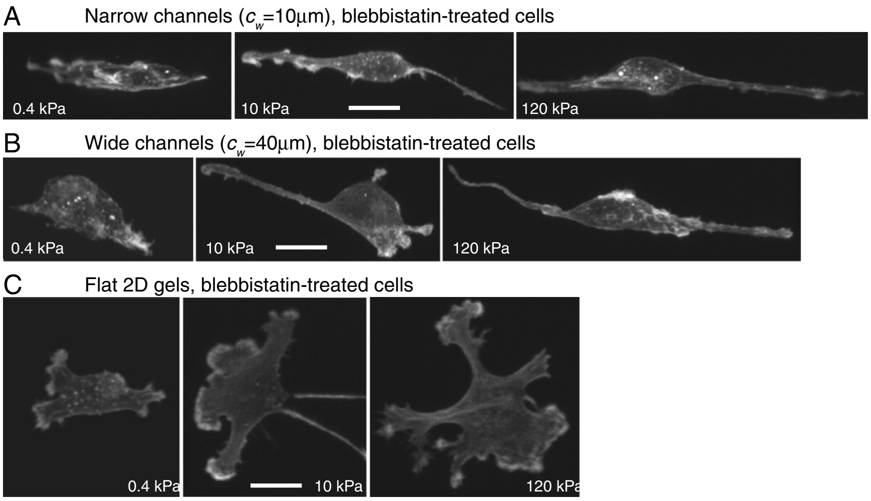

Fig. S4. Actin distribution of blebbistatin-treated cells in defined confinement. Confocal images of phalloidin-labeled F-actin distribution for blebbistatin-treated U373 cells in (*A*) narrow channels ($c_w = 10$ μm), (*B*) wide channels ($c_w = 40$ μm), and (*C*) unconfined flat 2D gels of varying ECM stiffness. F-actin distributions show reduced concentration of stress fibers in all ECM conditions. Scale bar = 20 μm.

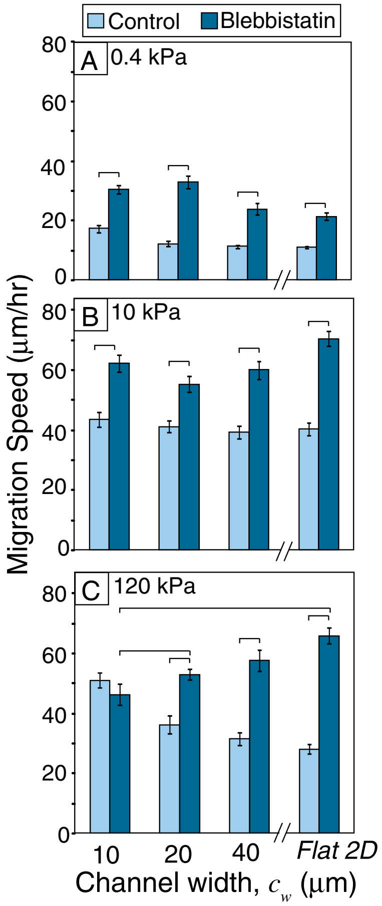

Fig. S5. Effect of nonmuscle myosin II inhibition on cell motility. Migration speed of blebbistatin-treated cells versus channel width for varying ECM stiffness and comparison with control measurements; n > 30 cells per condition. Statistically different groups ($p < 0.05$) indicated by horizontal square brackets.

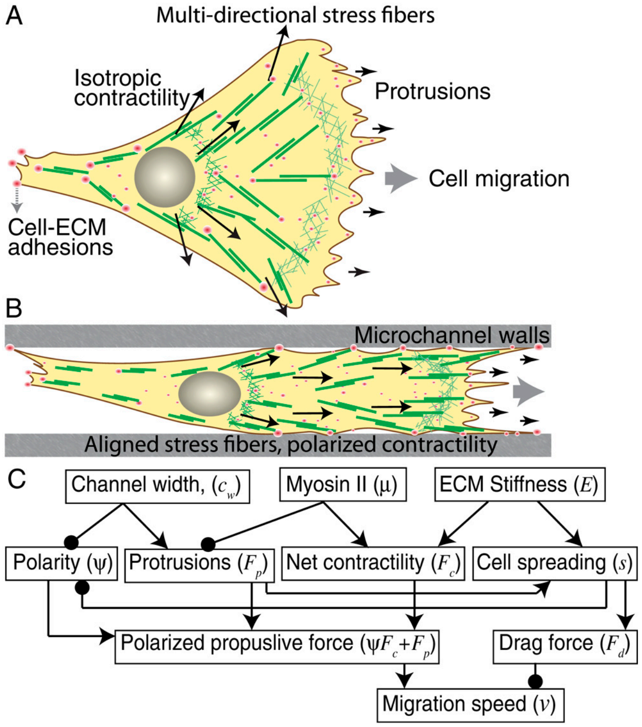

Fig. S6. Computational model. (*A*) Schematic of a cell spread on an unconfined (flat) 2D ECM depicting isotropic traction distribution, and (*B*) cell constrained inside a channel showing traction polarization along the direction of migration. (*C*) Relationships among cellular processes and corresponding modeling variables that affect cell migration speed.

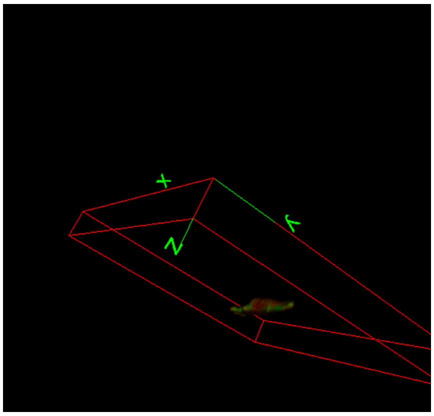

Movie S1. 3D reconstruction of a cell confined in a narrow channel. Volumetric 3D reconstruction of actin (green) and vinculin (red) distributions of a cell confined in a narrow channel ($c_w = 10$ μm) fabricated from 120 kPa PA hydrogel shows the cell adhered along the walls of the channel. The long axis of the channel is oriented along the *x* axis, the channel width is oriented along the *y* axis, and height is oriented along the *z* axis, with the bottom surface of the channel toward +*z*.

Movie S1 (AVI)

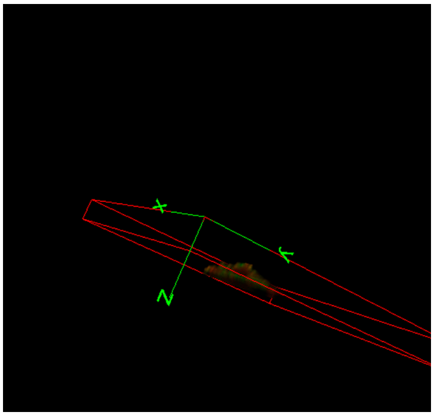

Movie S2. 3D reconstruction of a cell inside in a wide channel. Volumetric 3D reconstruction of actin (green) and vinculin (red) distributions of a cell confined in a wide channel ($c_w = 40$ μm) fabricated from 120 kPa PA hydrogel shows the cell adhered along the walls and spread on the bottom surface of the channel. The long axis of the channel is oriented along the *x* axis, the channel width is oriented along the *y* axis, and height is oriented along the *z* axis, with the bottom surface of the channel toward +z.

Movie S2 (AVI)